The Astrophysical Journal Letters, 903:L27 (7pp), 2020 November 10 https://doi.org/10.3847/2041-8213/abbee5
© 2020. The American Astronomical Society. All rights reserved.

Orbital Foregrounds for Ultra-short Duration Transients

Hank Corbett[1], Nicholas M. Law[1], Alan Vasquez Soto[1], Ward S. Howard[1], Amy Glazier[1], Ramses Gonzalez[1], Jeffrey K. Ratzloff[1], Nathan Galliher[1], Octavi Fors[1,2], and Robert Quimby[3,4]
[1] University of North Carolina at Chapel Hill, 120 E. Cameron Ave., Chapel Hill, NC 27514, USA; htc@unc.edu
[2] Institut de Ciències del Cosmos (ICCUB), Universitat de Barcelona, IEEC-UB, Martí i Franquès 1, E-08028 Barcelona, Spain
[3] San Diego State University, 5500 Campanile Dr., San Diego, CA 92182, USA
[4] Kavli Institute for the Physics and Mathematics of the Universe (WPI), The University of Tokyo Institutes for Advanced Study, The University of Tokyo, Kashiwa, Chiba 277-8583, Japan
Received 2020 September 16; revised 2020 October 5; accepted 2020 October 6; published 2020 November 5

Abstract

Reflections from objects in Earth orbit can produce subsecond, star-like optical flashes similar to astrophysical transients. Reflections have historically caused false alarms for transient surveys, but the population has not been systematically studied. We report event rates for these orbital flashes using the Evryscope Fast Transient Engine, a low-latency transient detection pipeline for the Evryscopes. We select single-epoch detections likely caused by Earth satellites and model the event rate as a function of both magnitude and sky position. We measure a rate of 1800^{+600}_{-280} sky^{-1} hr^{-1}, peaking at $m_g = 13.0$, for flashes morphologically degenerate with real astrophysical signals in surveys like the Evryscopes. Of these, 340^{+150}_{-85} sky^{-1} hr^{-1} are bright enough to be visible to the naked eye in typical suburban skies with a visual limiting magnitude of $V \approx 4$. These measurements place the event rate of orbital flashes orders of magnitude higher than the combined rate of public alerts from all active all-sky fast-timescale transient searches, including neutrino, gravitational-wave, gamma-ray, and radio observatories. Short-timescale orbital flashes form a dominating foreground for untriggered searches for fast transients in low-resolution, wide-angle surveys. However, events like fast radio bursts with arcminute-scale localization have a low probability ($\sim 10^{-5}$) of coincidence with an orbital flash, allowing optical surveys to place constraints on their potential optical counterparts in single images. Upcoming satellite internet constellations, like SpaceX Starlink, are unlikely to contribute significantly to the population of orbital flashes in normal operations.

Unified Astronomy Thesaurus concepts: Sky surveys (1464); Transient detection (1957); Wide-field telescopes (1800)

1. Introduction

Astrophysical phenomena with ultra-short (subminute) durations have largely escaped the scrutiny of modern synoptic sky surveys, which are typically optimized for supernovae-like transients evolving on day-to-month timescales. Sensitivity to minute- and hour-timescale events can be achieved through subsurveys over fractional sky areas; however, these searches typically use many-second exposures, confining the shortest events to single images.

Timescale limitations are less of a factor for multimessenger observatories, many of which operate with nearly continuous 4π sky coverage (Abbott et al. 2009; Bhat et al. 2009; IceCube Collaboration et al. 2017). In the past decade, optical surveys with nightly sky coverage approaching that of multimessenger facilities have come online, including the Evryscopes (Law et al. 2015; Ratzloff et al. 2019), the Mobile Astronomical System of Telescope-Robots (Lipunov et al. 2004), the Asteroid Terrestrial-impact Last Alert System (ATLAS; Tonry et al. 2018a), the All-Sky Automated Survey for Supernovae (ASAS-SN; Shappee et al. 2014), the Zwicky Transient Facility (Bellm et al. 2019), and the Multi-site All-Sky CAmeRA (Talens et al. 2017), opening up the rapid time domain considerably; however, any single-image transients in these surveys are hidden in a fog of known false positives, including particle strikes (Groom 2004) and reflected light from Earth satellites, which can exhibit a broad range of morphologies.

Image contamination by Earth satellites takes two forms: streaks, with uniform illumination over extended trajectories, and glints, which appear as short-duration flashes. These two morphologies are frequently degenerate, and depend on the structure and orbit of the reflector. Streaks are associated with fast-moving or slowly rotating satellites, such as the Starlink constellation discussed in McDowell (2020). Glints are associated with short rotation periods or high altitudes, and are produced by chance alignments between an observer, the Sun, and a reflective rotating surface. The duration of a glint is the crossing time of the reflective surface's normal vector across the disk of the Sun, less than a second for satellites with minutes-long rotation periods (Schaefer et al. 1987). Short durations relative to their motion on the sky and sharp contrast with their associated streaks have led to glints being mistaken for astrophysical events (Maley 1987, 1991; Schaefer et al. 1987; Rast 1991; Shamir & Nemiroff 2006).

Karpov et al. (2016) presents time-resolved observations of satellite glints that reveal a peak in the duration distribution at 0.4 s. Approximately half of the glints reported in Karpov et al. (2016) were not coincident with the position of a satellite in the NORAD database. Similarly, Tingay (2020) noted multiple candidates with no or poorly constrained association with tracked satellites based on their latest two-line element parameters. Based on these observations, it is unlikely that glints will be universally separable from a population of astrophysical transients based on ephemerides for tracked satellites.

The event rate and sky distribution of glints has not received systematic study, and the potential for these events to contaminate searches for ultra-short transients remains. In this Letter, we use single-image detections from the Evryscope Fast

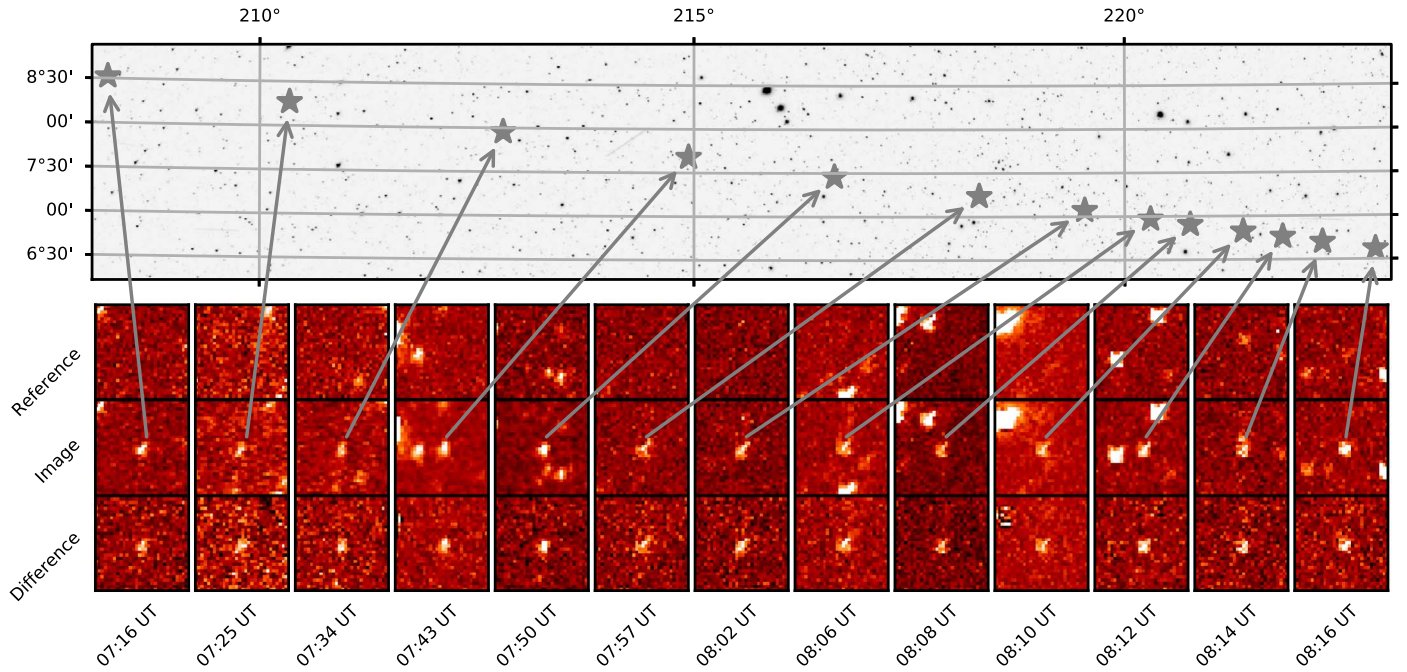

Figure 1. (Top) Example of a typical flash-producing trajectory seen by EFTE, followed over a single Evryscope pointing. (Bottom) Postage stamp cutouts of the reference, science, and discovery images, demonstrating point-like morphology. Each cutout is 30 × 30 pixels (6.6 × 6.′6) in size.

Transient Engine (Section 2) to measure the on-sky event rates of satellite glints for the first time. We provide estimates of the flash rate as a function of observed magnitude and sky position (Section 3). We discuss the impact of this population on both current and upcoming observatory facilities, and its implications for searches for ultra-short and multimessenger transients, including the hypothesized optical counterparts to fast radio bursts (FRBs), in Section 4.

2. Observations and Survey

We used observations from the Evryscopes, a north–south pair of robotic all-sky telescopes, located at Cerro Tololo Inter-American Observatory (Chile) and Mount Laguna Observatory (California). The Evryscopes survey an instantaneous field of view (FOV) of 16,512 square degrees at 2 minute cadence with 13.″2 pixel^{-1} resolution. Images were collected between 2019 November 24 and 2020 April 16, and we have made no cuts for weather. Images within 10° of the moon are excluded. The Evryscope system design and survey strategy are described in Ratzloff et al. (2019) and Law et al. (2015).

The Evryscope Fast Transient Engine (EFTE) is a detection pipeline developed for low-latency discovery of fast astrophysical transients, including bright flares from cool dwarfs (Howard et al. 2018, 2019), early phases of optical counterparts to gravitational wave events (Corbett et al. 2019), and the hypothesized optical counterparts to FRBs (Lyutikov & Lorimer 2016; Yang et al. 2019; Chen et al. 2020).

2.1. Single-epoch Flash Sample

We observed 3,372,044 high-probability candidates that passed our vetting criteria as described in Section 2.2. Of these, we identify 1,415,722 candidates that do not appear in multiple epochs as likely satellite flashes. This cut removes variable stars and persistent artifacts from bright stars.

Single-epoch candidates tend to occur in tracks across the sky on timescales ranging from subcadence to hours. Figure 1 shows a typical track observed by Evryscope, followed for 1 hr, along with typical 30 × 30 pixel (6.6 × 6.′6) subtraction stamps from the EFTE pipeline. The timescale of the delay between flashes gives an angular speed of 10″ s^{-1}, or roughly one Evryscope pixel per second. However, we do not observe any streaking at any epoch, implying that the duration of each individual flash is much less than 1 second. This is consistent with the population of fast optical flashes noted in Biryukov et al. (2015) and Karpov et al. (2016), but observed in images integrated over minutes.

2.2. Transient Detection with the Evryscopes

EFTE uses a simplified image-subtraction technique for candidate detection. Evryscope focus and optics, and thus PSFs, are stable on month-to-year timescales (Ratzloff et al. 2020), and atmospheric seeing is dominated by optical effects under all observing conditions in each Evryscope's 13.″2 pixels. This stability means that image subtraction within a single pointing does not require the PSF-matching techniques addressed by standard routines, such as HOTPANTS (Becker 2015) or ZOGY (Zackay et al. 2016). Similarly, because we are targeting the fastest-timescale events, we do not require widely spaced reference frames; instead, an earlier image from the same pointing is subtracted from each image, typically with a 10 minute separation.

For each single-camera science image $S(x, y)$ and reference image $R(x, y)$, we calculate a discovery image $D(x, y)$ from the per-pixel change in signal-to-noise ratio. Both $S(x, y)$ and $R(x, y)$ are calibrated, background-subtracted, and aligned images in electron units. We measured image background levels using an interpolated and clipped mesh, as implemented in SEXTRACTOR (Bertin & Arnouts 1996). The discovery image $D(x, y)$ is given by:

$$D(x, y) = \frac{S(x, y)}{s_S(x, y)} - \frac{R(x, y)}{s_R(x, y)}, \quad (1)$$

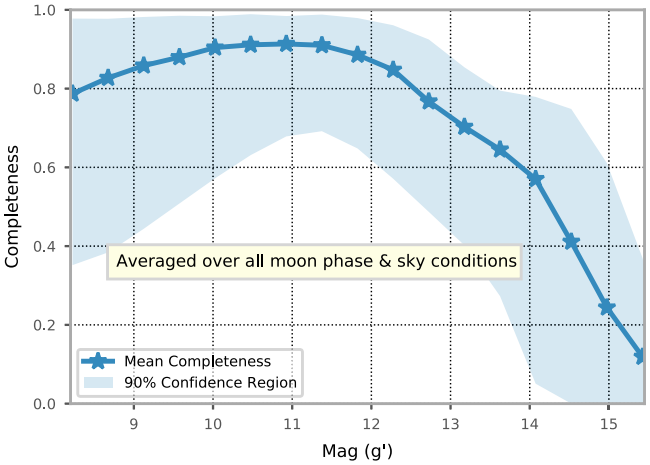

Figure 2. Completeness vs. magnitude for the Evryscope Fast Transient Engine (EFTE) pipeline, averaged over all observing conditions and cameras.

where $s_R(x, y)$ and $s_S(x, y)$ are noise images calculated for each image $I(x, y)$ with measured background noise $s_B^2(x, y)$ as

$$s_I(x, y) = \sqrt{I(x, y) + s_B^2(x, y)}. \quad (2)$$

While this technique is not statistically optimal, it is efficient (98.5% of images are reduced in cadence) and produces stable artifacts that can be rejected via automated means. We identified all sources where $D(x, y) \geqslant 3$ in at least three contiguous pixels for automated vetting. We perform aperture photometry for all candidates using the science image, and calibrated the results to the ATLAS All-Sky Stellar Reference Catalog (Tonry et al. 2018b).

A typical single image subtraction using this method produces $O(10^3)$ candidates. We require the ratio of negative-to-positive pixels within a 5 pixel diameter to be less than 0.3 to remove dipole artifacts from misalignments and Poisson noise peaks near bright stars, which reduces the number of candidates to $O(10^2)$. These are then processed with a convolutional neural network (LeCun et al. 1998) trained on small cutouts from $S(x, y)$, $D(x, y)$, and $R(x, y)$ in both real and simulated data, reducing the final number of candidates to 6^{+13}_{-5} per image when averaged over all weather conditions and cameras.

2.3. Survey Completeness

We characterized the completeness of the EFTE survey with injection-recovery testing. The image sample contained 500 pairs with the same 10 minute separation used on-sky, and was representative of all weather and instrument conditions contained in the survey. We injected ∼1200 sources into each image ($8.0 \leqslant m_{g'} \leqslant 16.75$), using the normalized median of nearby stars as the injection PSF. We processed each image pair as described in Section 2.2 twice, alternating which image in the pair was used as the science frame. We define a recovery as a candidate detected within three pixels of an injection position, with the radius determined by the 99th percentile of the nearest-neighbor distance between the vetted candidates and their nearest injection position.

Figure 2 shows the measured completeness as a function of magnitude, along with the 90% confidence interval (CI), which includes measurement uncertainty, variability with observing conditions, and the vignetting effects. Completeness decreases at both the bright and dim ends of the distribution. Saturation causes poorly constrained centroids leading to nonrecovery at the bright end. The average 50% completeness limit of $m_{g'} = 14.2$ is brighter than the Evryscope dark-sky, single-image limit of $m_{g'} = 16$ due to a combination of including all-sky conditions in our analysis and using reference images with similar noise profiles to science images.

2.4. Candidate Reliability

Despite careful vetting, the median EFTE false positive rate is ∼6800 per hr. In EFTE surveys for rapidly evolving transients, further vetting is performed by crossmatching with galaxy and stellar catalogs, or by association with gamma-ray and gravitational-wave transient skymaps, combined with direct human interaction. Measuring an all-sky event rate, however, requires knowing the fraction of real events in the sample. To measure this fraction, we visually inspected 27,817 randomly selected single-epoch candidates that passed our automated vetting as described in Section 2.2.

Each candidate was assigned a binary classification, where a *real* classification corresponds to a candidate that is morphologically consistent with an astrophysical transient. Of the candidates classified, 2823 were classified as real. From this, we estimate the real flash fraction (RFF) in the vetted EFTE event stream to be 0.10 ± 0.03. Least-squares fits to the RFF as a function of magnitude and solar elongation produced slopes not different from zero, with an uncertainty set by the standard deviation of the residuals around the fit. Bogus candidates included:

1. Subtraction artifacts from bright stars (50%).
2. Optical ghosts, distinguished based on non-PSF-like shapes and presence in the reference frame (1%).
3. Aircraft strobes, distinguished based on nearby parallel streaks (3%).
4. Particle strikes (46%).

The final category includes both readily identifiable cosmic-ray muon tracks and signals caused by Compton recoil electrons from environmental radioisotopes, which can be PSF-like. To constrain this population, we reduced a series of 120 s darks with EFTE and searched for candidates meeting our vetting criteria. We place an upper limit on the base rate of PSF-like particle strikes of $\leqslant$0.1 per image, or ∼300 sky^{-1} hr^{-1}, which is small compared to the all-sky orbital flash rate (Section 3.2).

Evryscope PSFs, and the resulting degree to which stellar sources are undersampled, are variable across each individual camera's FOV. At the center of the field, dim sources can have an FWHM $\ll$ 1 pixel. To avoid distortion of these sources, we estimate the prevalence of particle strikes in our candidate sample using the RFF, rather than directly removing them from the images with standard cosmic-ray mitigation tools, such as LA-Cosmic (van Dokkum 2001).

3. Event Rates of Flash Events

We calculated event rates for candidates within discrete bins in observed magnitude in a 2 minute integration. Raw event rates for each magnitude bin $r(m_o)$ are given by:

$$r(m_o) = \frac{F_m}{c_i f_i N_i}, \quad (3)$$

where F_m and N_i are the number of candidates observed within the magnitude bin and the number of images in the survey, respectively, c_i is the coverage per image, and f_i is the fill fraction of each image (i.e., the fraction of a single camera FOV that contributes to the overlap-deduplicated Evryscope FOV). Per-image coverage is constant at $c_i = 12.348\ \mathrm{deg}^2$ hr. The fill fraction is determined by camera arrangement ($f_i = 0.965$).

3.1. Monte Carlo Rate Correction

We used a Monte Carlo approach to model the effects of completeness and reliability as a function of magnitude (Section 2.3). We modeled the per-magnitude completeness as a bounded Johnson distribution (Johnson 1949) using maximum likelihood estimates for the mean, standard deviation, skewness, and kurtosis from injection testing. We corrected for the reliability of the event sample using the RFF described in Section 2.4, modeled per magnitude bin as a normal distribution.

For each magnitude bin, we made 100,000 draws from the fitted completeness and reliability distributions, each time calculating a corrected event rate as

$$\Gamma(m_o)_i = \frac{r_{m_o} R_i}{C_i}, \tag{4}$$

where C and R represent values drawn from the completeness and reliability distributions, respectively. The reported mean rate is the 50th percentile of $\Gamma(m_o)_i$. The lower and upper bounds of the 90% CI were taken to be the 5th and 95th percentiles of $\Gamma(m_o)_i$.

3.2. Magnitude Distribution

As noted in Lyutikov & Lorimer (2016), flashes shorter than an image exposure time (typically $\gg$1 second) will exhibit phase blurring, diluting their flux relative to the surrounding stars by the ratio of the integration time to their intrinsic duration. For subsecond durations, consistent with the example seen in Figure 1 and in Biryukov et al. (2015), the peak of the flash light curve will be brighter than observed in long integrations. In general, the peak magnitude of the flash m_P is given by

$$m_P = -2.5 \log_{10}\left(\frac{T_{exp} 10^{-0.4 m_o}}{\tau_f}\right), \tag{5}$$

where τ_f is the equivalent width of the light curve and T_{exp} is the exposure time. We assume a flash duration of 0.4 s, based on the mode of the distribution presented in Karpov et al. (2016), when estimating the peak brightness from the observed magnitude.

Figure 3 shows the cumulative and normalized magnitude density distributions as a function of observed and estimated peak brightness. The shaded regions represent the 90% CI. For the cumulative distributions, the CI is bounded by the cumulative quadrature sum of the per-bin CI limits. We extrapolate an all-sky event rate from the observed rates in three regions: around the south celestial pole (SCP), within 10° of the equator, and across all declinations. Both the all-sky and equatorial distributions peak at $m_o = 13$, whereas the polar distribution peaks at $m_o = 12.2$, with a possible second peak near the saturation limit.

We measured integrated flash rates for $m_o < 14.25$ of $1.0^{+0.27}_{-0.15} \times 10^3$, $4.0^{+1.40}_{-0.60} \times 10^3$, and $1.8^{+0.60}_{-0.28} \times 10^3$ sky^{-1} hr^{-1} in the SCP, equatorial, and averaged all-sky regions, respectively. Assuming that the observed population is dominated by satellite glints, we expect a higher rate near the equator because equatorial orbits are confined to a narrow decl. band. The SCP region will only contain objects in polar orbits spanning the full decl. range, lowering the observed rate.

3.3. Solar Geometry Dependence

If the observed flashes are caused by reflections from satellites, none should be expected from the region of the sky covered by Earth's shadow. The solid angle subtended by the shadow depends on satellite altitude, following the geometry illustrated in Figure 4. For low-Earth orbit (LEO) altitudes (<2000 km), the shadow covers a 50° radius around the solar antipode. The angular size shrinks to a 14° radius for medium-Earth orbit (MEO), or a 9° radius for geosynchronous orbit. We evaluated the distance between each of the human-vetted candidates from Section 2.4 and the solar antipode. Shaded regions depict the angular extent of Earth's shadow for LEO, MEO, and geosynchronous satellites.

The prevalence of flashes decreases steadily with proximity to the shadow in the region covered for LEO objects, before falling in the solid angle covered for MEO and higher orbits. Approximately 34% of the flashes occurred within 50° of the center of the shadow. Few flashes occur within the region within Earth's shadow for MEO and geosynchronous orbits, with 3.5% within 14° of the antipode and only 1.1% within 9°, which suggests that the majority of the flashes are generated by satellites in middle- and high-Earth orbit. No Evryscope observations occur within ~80° of the Sun.

4. Implications for Fast Transient Searches

Earth satellites produce thousands of potential false alarms mimicking fast transients. One option to mitigate this fog is to duplicate monitoring across a substantial (~3 kilometer for Evryscope-scale resolution) baseline, enabling parallax-based coincidence rejection. However, this requires construction of multiple facilities. An alternative approach is to track glint-producing objects directly in the event stream, using calculated orbit fits to reject candidates that occur in tracks. This approach is currently in development for the EFTE event stream (A. Vasquez Soto et al. 2020, in preparation).

Degradation of the night sky by *megaconstellations* of LEO satellites is anticipated to be a major environmental challenge for astronomy in the coming decade (McDowell 2020). The construction of these constellations will increase the number of artificial satellites in orbit by a factor of many, with a corresponding increase in the amount of reflected sunlight visible in astronomical images. However, due to their high angular speeds and controlled rotation, reflected light from satellites similar to Starlink is unlikely to produce PSF-like glints during normal operations.

4.1. Visual Observers

The all-sky magnitude distribution in Figure 3 shows that the instantaneous peak brightness of many flashes should be detectable to the unassisted human eye. For a typical suburban sky with limiting magnitude $V \approx 4$, we predict a naked-eye-visible event rate of 340^{+150}_{-85} sky^{-1} hr^{-1} based on the all-sky

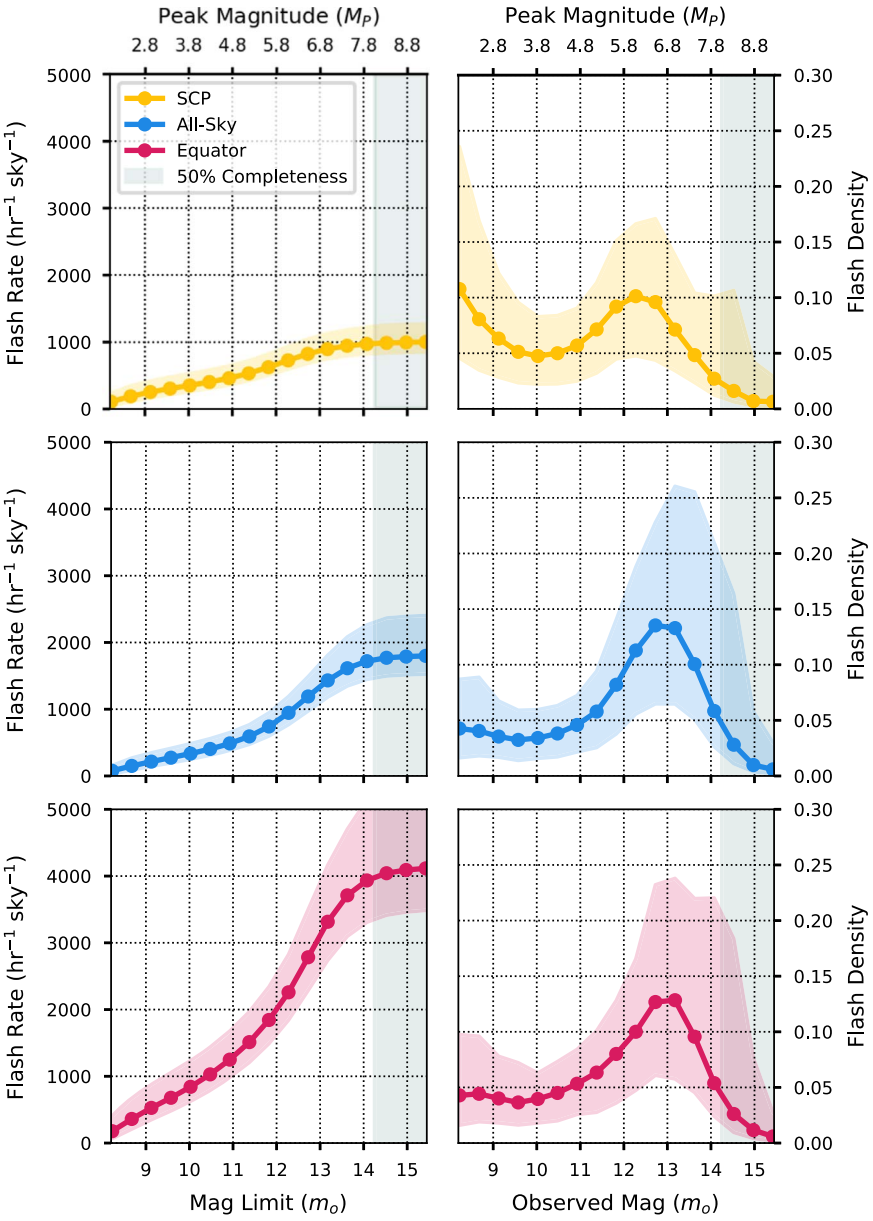

Figure 3. Cumulative (left) and normalized (right) flash rate distributions as a function of magnitude. We consider the event rate around the south celestial pole (SCP; top), averaged across the sky (center), and around the equator (bottom) as a function of both observed magnitude in 120 s integrations and limiting peak magnitudes assuming a 0.4 s flash duration. Rates are corrected using the technique described in Section 3.1 to account for survey completeness and contamination. Shaded region gives the 90% CI on each distribution.

averaged cumulative event rate of $1.8^{+0.60}_{-0.28} \times 10^3$ sky^{-1} hr^{-1} ($m_o < 14.25$). At the darkest sky sites, with limiting magnitude $V \approx 6$, this rate increases to 740^{+200}_{-140} sky^{-1} hr^{-1}. Within the equatorial region, the expected naked-eye event rate increases to 840^{+390}_{-220} sky^{-1} hr^{-1} ($V \approx 4$), or 1800^{+500}_{-350} sky^{-1} hr^{-1} ($V \approx 6$), based on the cumulative equatorial event rate of $4.0^{+1.40}_{-0.60} \times 10^3$ sky^{-1} hr^{-1}.

The time resolution (Cornsweet 2014) and biochemical adaptation time (Yeh et al. 1996; Dunn & Rieke 2006) of the human eye are comparable to orbital flash durations. We expect the naked-eye detectability of these flashes to vary strongly with observer ability.

4.2. Narrow-field Imaging

The impact of orbital flashes on narrow-field imagers is negligible. For a $10 \times 10'$ FOV, we predict approximately 1.2 flashes per 1000 hr of exposure time based on the all-sky averaged event rate, or 2.7 flashes per 1000 hr of exposure time based on the equatorial region event rate. While these are relatively rare events, they could account for occasional flashes that have been remarked on by amateur astronomers and some rejected single-image detections in tiling sky surveys.

4.3. Multimessenger Coincidence Searches

The flash rate measured here also implies a high coincidence rate for multimessenger events. The Canadian Hydrogen Intensity Mapping Experiment (CHIME) is able to localize FRBs to the nearest arcminute (The CHIME/FRB

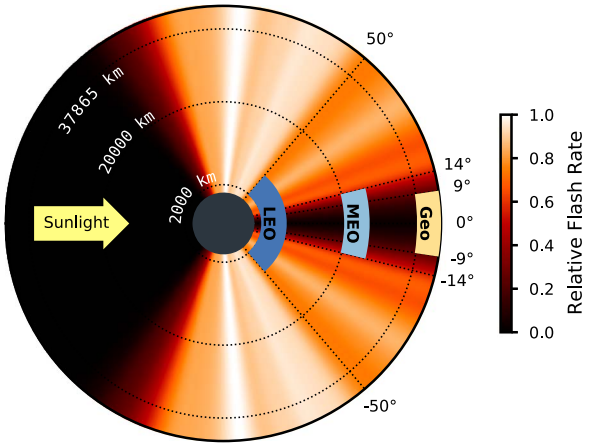

Figure 4. Geometry of Earth's shadow relative to the position of the solar antipode. The angular size of the shadow depends on altitude, ranging from 9° for a typical geosynchronous orbit, to 50° at the upper limit of low-Earth orbit. The color gradient represents a kernel density estimation for the relative flash rate as a function of antipode distance based on the visually sorted sample from Section 2.4, and is reflected across the Sun–Earth axis.

Collaboration et al. 2018), reducing the expected flash count within the error radius to a likely acceptable 3.8×10^{-5} hr^{-1} based on the all-sky averaged event rate. Wide-angle surveys like Evryscope can be expected to have a false alarm rate (FAR) of 1 per 3 yr for apparent FRB optical counterparts due to orbital flashes. For FRBs localized to the equatorial region, the expected event rate and FAR increase to 8.5×10^{-5} hr^{-1} and 1 per 1.3 yr, respectively.

In contrast, gamma-ray bursts (GRBs) from the Fermi Gamma Burst Monitor have a median 90% localization area of 209 square degrees (Goldstein et al. 2020), leading to an expected flash count of 9.1 hr^{-1} based on the all-sky averaged cumulative event rate. With simultaneous coverage and physical constraints on the timescale of the optical component, the expected flash count drops to 0.15 minute^{-1}. For GRB localizations within the equatorial region, the rates increase to 20 hr^{-1}, or 0.33 minute^{-1}.

Events with larger localization regions or weakly constrained early lightcurves, like gravitational wave events from LIGO/Virgo, will be more heavily impacted. For a typical 1200 sq. degree sky map, the expected flash is 53 hr^{-1} assuming the all-sky averaged event rate, or 120 hr^{-1} within the equatorial region. The resulting FAR will increase linearly with both localization area and trigger rate.

4.4. Vera C. Rubin Observatory

We predict that point-like flashes will occur in images from Vera C. Rubin Observatory at a rate of 6.4×10^{-4} flashes per image (15 s of 3.5 square degrees), based on the all-sky averaged event rate. Assuming $O(1000)$ pointings, we expect Rubin to observe on the order of 1.3 flashes per night from this population. In the worst case scenario of all pointings being confined to the equatorial region, this rate increases to 1.4×10^{-3} flashes per image, or 2.8 flashes per night. Due to the 15 s exposure time of Rubin, the average observed magnitude of the flash distribution will be shifted to $m_g \sim 10.7$, 100× brighter than the g-band bright limit of $m_g = 15.7$ (LSST Science Collaboration et al. 2009). Our observed magnitude distribution drops off at the faint end, but there is the potential for a second distribution to exist beyond the Evryscope depth limit, as is seen for geosynchronous debris observed by the DebrisWatch survey (Blake et al. 2020).

We estimate that a worst-case scenario 10 millisecond flash from a geosynchronous satellite will produce a 0.″15 streak, likely indistinguishable in Rubin's 0.″2 pixels. Longer-duration flashes, like the 0.4 s events we have assumed here, would produce obvious 6″ streaks. However, fully constraining the expected morphology of orbital flashes in Rubin data will require modeling of their duration via orbital characteristics of the population.

The Evryscope was constructed under National Science Foundation ATI grant AST-1407589, with operating costs from National Science Foundation CAREER grant 1555175. Current operations are supported by AAG-2009645. H.C. was supported by the National Science Foundation Graduate Research Fellowship (grant No. DGE-1144081), AAG-2009645, and the North Carolina Space Grant. O.F. acknowledges the support by the Spanish Ministerio de Ciencia e Innovación (MICINN) under grant PID2019-105510GB-C31 and through the "Center of Excellence María de Maeztu 2020–2023" award to the ICCUB (CEX2019-000918-M). This research made use of Astropy,[5] a community-developed core Python package for Astronomy (Astropy Collaboration et al. 2013, 2018), and SciPy,[6] a core Python package for general scientific computing tasks.

ORCID iDs

Hank Corbett https://orcid.org/0000-0002-6339-6706
Nicholas M. Law https://orcid.org/0000-0001-9380-6457
Alan Vasquez Soto https://orcid.org/0000-0002-1906-1167
Ward S. Howard https://orcid.org/0000-0002-0583-0949
Amy Glazier https://orcid.org/0000-0001-9981-4909
Ramses Gonzalez https://orcid.org/0000-0001-5083-8272
Jeffrey K. Ratzloff https://orcid.org/0000-0001-8791-7388
Nathan Galliher https://orcid.org/0000-0001-8105-1042
Octavi Fors https://orcid.org/0000-0002-4227-9308
Robert Quimby https://orcid.org/0000-0001-9171-5236

References

Abbott, B. P., Abbott, R., Adhikari, R., et al. 2009, RPPh, 72, 076901
Astropy Collaboration, Price-Whelan, A. M., Sipőcz, B. M., et al. 2018, AJ, 156, 123
Astropy Collaboration, Robitaille, T. P., Tollerud, E. J., et al. 2013, A&A, 558, A33
Becker, A. 2015, HOTPANTS: High Order Transform of PSF ANd Template Subtraction, Astrophysics Source Code Library, ascl:1504.004
Bellm, E. C., Kulkarni, S. R., Graham, M. J., et al. 2019, PASP, 131, 018002
Bertin, E., & Arnouts, S. 1996, A&AS, 117, 393
Bhat, P. N., Meegan, C. A., Lichti, G. G., et al. 2009, in AIP Conf. Ser. 1133, Gamma-ray Burst: Sixth Huntsville Symposium, ed. C. Meegan, C. Kouveliotou, & N. Gehrels (Melville, NY: AIP), 34
Biryukov, A., Beskin, G., Karpov, S., et al. 2015, BaltA, 24, 100
Blake, J. A., Chote, P., Pollacco, D., et al. 2020, AdSpR, in press (doi:10.1016/j.asr.2020.08.008)
Chen, G., Ravi, V., & Lu, W. 2020, ApJ, 897, 146
Corbett, H., Ackley, K., Law, N., et al. 2019, GCN, 26227, 1
Cornsweet, T. 2014, Visual Perception (New York: Elsevier)
Dunn, F. A., & Rieke, F. 2006, Current Opinion in Neurobiology, 16, 363
Goldstein, A., Fletcher, C., Veres, P., et al. 2020, ApJ, 895, 40

[5] http://www.astropy.org
[6] http://www.scipy.org

Groom, D. 2004, in Scientific Detectors for Astronomy, Astrophysics and Space Science Library Vol. 300, ed. P. Amico, J. W. Beletic, & J. E. Beletic (Berlin: Springer), 81
Howard, W. S., Corbett, H., Law, N. M., et al. 2019, ApJ, 881, 9
Howard, W. S., Tilley, M. A., Corbett, H., et al. 2018, ApJL, 860, L30
IceCube Collaboration, Aartsen, M. G., Ackermann, M., et al. 2017, JInst, 12, P03012
Johnson, N. L. 1949, Biometrika, 36, 149
Karpov, S., Beskin, G., Biryukov, A., et al. 2016, RMxAC, 48, 91
Law, N. M., Fors, O., Ratzloff, J., et al. 2015, PASP, 127, 234
LeCun, Y., Bottou, L., Bengio, Y., & Haffner, P. 1998, IEEEP, 86, 2278
Lipunov, V. M., Krylov, A. V., Kornilov, V. G., et al. 2004, AN, 325, 580
LSST Science Collaboration, Abell, P. A., Allison, J., et al. 2009, arXiv:0912.0201
Lyutikov, M., & Lorimer, D. R. 2016, ApJL, 824, L18
Maley, P. 1991, AdSpR, 11, 33
Maley, P. D. 1987, ApJL, 317, L39
McDowell, J. C. 2020, ApJL, 892, L36
Rast, R. H. 1991, Icar, 90, 328
Ratzloff, J. K., Law, N. M., Corbett, H. T., Fors, O., & del Ser, D. 2020, JATIS, 6, 018002
Ratzloff, J. K., Law, N. M., Fors, O., et al. 2019, PASP, 131, 075001
Schaefer, B. E., Barber, M., Brooks, J. J., et al. 1987, ApJ, 320, 398
Shamir, L., & Nemiroff, R. J. 2006, PASP, 118, 1180
Shappee, B. J., Prieto, J. L., Grupe, D., et al. 2014, ApJ, 788, 48
Talens, G. J. J., Spronck, J. F. P., Lesage, A. L., et al. 2017, A&A, 601, A11
The CHIME/FRB Collaboration, Amiri, M., Bandura, K., et al. 2018, ApJ, 863, 48
Tingay, S. 2020, PASA, 37, e015
Tonry, J. L., Denneau, L., Flewelling, H., et al. 2018b, ApJ, 867, 105
Tonry, J. L., Denneau, L., Heinze, A. N., et al. 2018a, PASP, 130, 064505
van Dokkum, P. G. 2001, PASP, 113, 1420
Yang, Y.-P., Zhang, B., & Wei, J.-Y. 2019, ApJ, 878, 89
Yeh, T., Lee, B. B., & Kremers, J. 1996, Vision Research, 36, 913
Zackay, B., Ofek, E. O., & Gal-Yam, A. 2016, ApJ, 830, 27